

DFT insights into the electronic structure, mechanical behaviour, lattice dynamics and defect processes in the first Sc-based MAX phase Sc₂SnC

M. A. Hadi (✉ hadipab@gmail.com)

University of Rajshahi

S.-R. G. Christopoulos

Coventry University

A. Chroneos

University of Thessaly

S. H. Naqib

University of Rajshahi

A. K.M.A. Islam

University of Rajshahi

Research Article

Keywords: sc₂snc, m₂snc, family, properties, phases

Posted Date: September 8th, 2021

DOI: <https://doi.org/10.21203/rs.3.rs-870934/v1>

License:  This work is licensed under a Creative Commons Attribution 4.0 International License.

[Read Full License](#)

DFT insights into the electronic structure, mechanical behaviour, lattice dynamics and defect processes in the first Sc-based MAX phase Sc₂SnC

M.A. Hadi^{1*}, S.-R.G. Christopoulos², A. Chroneos^{3,4}, S.H. Naqib¹, A.K.M.A. Islam^{1,5}

¹Department of Physics, University of Rajshahi, Rajshahi 6205, Bangladesh

²Faculty of Engineering, Environment and Computing, Coventry University, Priory Street, Coventry CV1 5FB, UK

³Department of Electrical and Computer Engineering, University of Thessaly, 38221 Volos, Greece

⁴Department of Materials, Imperial College, London SW7 2AZ, UK

⁵International Islamic University Chittagong, Kumira, Chittagong-4318, Bangladesh

*Correspondence: hadipab@gmail.com

Abstract

The ceramic and metallic properties of the MAX phases make them attractive for numerous technological applications. The very recent experimental synthesis of the first scandium (Sc) based MAX phase Sc₂SnC is an important addition to the MAX phase family as it further expands the diversity of physical characteristics of this family. Here we employ density functional theory (DFT) calculations to investigate the structural, electronic, mechanical, lattice dynamical properties of Sc₂SnC including defect processes to compare with those of existing M₂SnC phases. The calculated structural properties are in good agreement with the experimental values. The new phase Sc₂SnC is structurally, mechanically and dynamically stable. Sc₂SnC is metallic with a mixture of covalent and ionic character. The covalency of Sc₂SnC including M₂SnC is mostly controlled by the effective valence. Sc₂SnC in M₂SnC family ranks second in the scale of deformability, softness and machinability. The elastic anisotropy level in Sc₂SnC is moderate compared to the other M₂SnC phases. Like other members of the M₂SnC family, Sc₂SnC has the potential to be etched into 2D MXenes and has the potential to be a thermal barrier coating (TBC) material. The hardness and melting point of Sc₂SnC, including M₂SnC, follows the trend of bulk modulus.

Introduction

Compounds of the ternary laminated family, discovered six decades ago as the H-phases, are now referred to as the MAX phases^{1,2}. This family is chemically represented by M_{n+1}AX_n, where M is a transition metal, A is an A-group element and X is either carbon or nitrogen or boron³. The integer *n* is called the layer index of the M atom. According to *n*, the MAX family is divided into six sub-families so far, such 211, 312, 413, 514, 615, and 716 MAX phases³. This family has also been described as metallic ceramics as they combine some metallic and ceramic properties³. Similar to metals, some MAX phases are electrically and thermally conductive, resistant to thermal shock, damage tolerant, and readily machinable. Again, they resemble ceramics, as some of them are lightweight, wear resistant, elastically rigid, brittle, and resistant to oxidation and corrosion.

The crystal structure of MAX phases consists of nearly close-packed layers of MX₆ octahedra interpolated with square-planar slabs of A-atomic layers. In these the X atoms occupy the octahedral sites between the M-atoms. The A atoms reside in the center of trigonal prisms, which are slightly larger than the octahedral sites so as to better accommodate the relatively large A-atoms⁴. The interposing pure A-element planes are mirror planes to the zigzagging M_{n+1}X_n-slabs. Alternatively, the structure of the MAX phases consists of highly symmetrical unit cells that are atomically layered along the *c*-axis. In the unit cell, the (*n*+1) ceramic MX-layers are stacked along the *c*-axis between the two metallic A-layers. The thickness of these atomic layers is within the nanometer range and this is the reason MAX phases are sometimes termed as nanolaminates. The periodic arrangement of the metallic and ceramic layers is responsible for the metallic and ceramic properties of the MAX

phases. MAX phases have numerous potential applications ranging from aerospace to nuclear reactors⁵. Recently, MAX phases are used to derive the two-dimensional MXenes, which are being used as energy storage materials and as electrodes in electrochemical capacitors, micro-supercapacitors, and batteries⁶.

Interest in the Sn-containing MAX phase is high in the community due to the report on attractive electrochemical performance of Nb₂SnC in Li-ion electrolytes⁷. Importantly, two of the three MAX phases discovered after this report are Sn-based MAX Phases. These new members in MAX family are V₂SnC⁸, Zr₂SeC⁹, and Sc₂SnC¹⁰. The last one is the first Sc-based MAX phase reported with full crystallographic information. Previously, Sc₂InC was included into a list for H-phases, however, without any crystallographic data¹¹. The source was mentioned as private communication. Up to now there is no experimental evidence of synthesis and characterization of Sc₂InC. Therefore, it can be inferred that Sc₂SnC is the first Sc-based compound in MAX family. Sc₂SnC is also exceptional for another reason. The M-element Sc of Sc₂SnC is a rare-earth element, which, in general, in the MAX compounds is typically a transition metal. This uniqueness of Sc₂SnC encouraged the present DFT investigation. Here we aim to calculate the structural, electronic, mechanical, and thermal properties including Vickers hardness and defect processes of Sc₂SnC. The derived properties are compared with those found for previously synthesized other M₂SnC MAX phases.

Computational methods

The present DFT calculations were performed using the CASTEP code¹². The Perdew-Burke-Ernzerhof (PBE) functional within the generalized gradient approximation (GGA) was used to evaluate the electronic exchange-correlation energy¹³. Ultra-soft pseudo-potential proposed by Vanderbilt is chosen to model the interactions between electrons and ion cores¹⁴. The Monkhorst-Pack (MP) scheme with a Γ -centered k-point mesh of 15×15×3 grid is employed to integrate over the first Brillouin zone in the reciprocal space of hexagonal unit cell of Sc₂SnC¹⁵. A cutoff energy of 700 eV is preferred to expand the eigenfunctions of the valence and nearly valence electrons using a plane-wave basis. During the geometry optimization, both the total energy and internal forces are minimized with the Broyden-Fletcher-Goldfarb-Shanno (BFGS) algorithm¹⁶. To achieve the self-consistent convergence the difference in the total energy is kept less than 5×10⁻⁶ eV/atom, the maximum ionic Hellmann-Feynman force less than 0.01 eV/Å, maximum ionic displacement less than 5×10⁻⁴ Å, and maximum stress less than 0.02 GPa.

The elastic properties are investigated within the first-principles method using finite-strain theory embedded in the CASTEP code¹⁷. In this method, a predetermined value for strain is used to relax all the free parameters and compute the stress. For elastic calculations, the convergence criteria are set as: the difference in total energy less than 10⁻⁶ eV/atom, the maximum ionic Hellmann-Feynman force less than 2×10⁻³ eV/Å, and the maximum ionic displacement less than 10⁻⁴ Å. The finite-strain theory as implemented in CASTEP has been successfully employed to calculate the elastic properties of numerous systems¹⁸⁻²⁹.

Lattice dynamic properties such as phonon dispersion and phonon density of states are calculated using a 3×3×1 supercell employing the finite displacement supercell method within the code. A 35×35×7 k-point mesh was used to calculate the electronic charge density distribution and the Fermi surface. Defect calculations were carried out with a supercell of 72-atomic site (36M, 18A, and 18 C) using a 3×3×1 grid k-point mesh within the MP scheme under constant pressure. To determine the potential interstitial sites a thorough computational search was performed examining all potential interstitial sites.

Results and discussions

Structural properties: Commonly with other MAX phases Sc₂SnC crystallizes in the hexagonal space group *P6₃/mmc* (No. 194). Each unit cell of Sc₂SnC contains two formula units and eight atoms (refer to Figure 1(a)). The Sc atoms occupy the 4*f* Wyckoff site with the fractional coordinates (1/3, 2/3, z),

the Sn resides in the $2d$ atomic site with the fractional coordinates $(1/3, 2/3, 3/4)$ and the C atoms take position at the $2a$ Wyckoff position with the fractional coordinates $(0, 0, 0)$. The optimized lattice parameters are listed in Table S1 in the supplementary section along with those of all M_2SnC MAX phases including experimental values^{8,10,30–32}. The present values for Sc_2SnC show very good agreement with the experimental values, suggesting the validity of the present investigation. In previous studies^{30,31}, we observed that the lattice constants of Sn-based 211 MAX phases maintain a good relation with the crystal radius of M-atoms. Both lattice constants a and c increase almost linearly with the crystal radius of M-atoms. The Sn-based new compound Sc_2SnC also maintains this relationship (see Figure 1(b) and (c)).

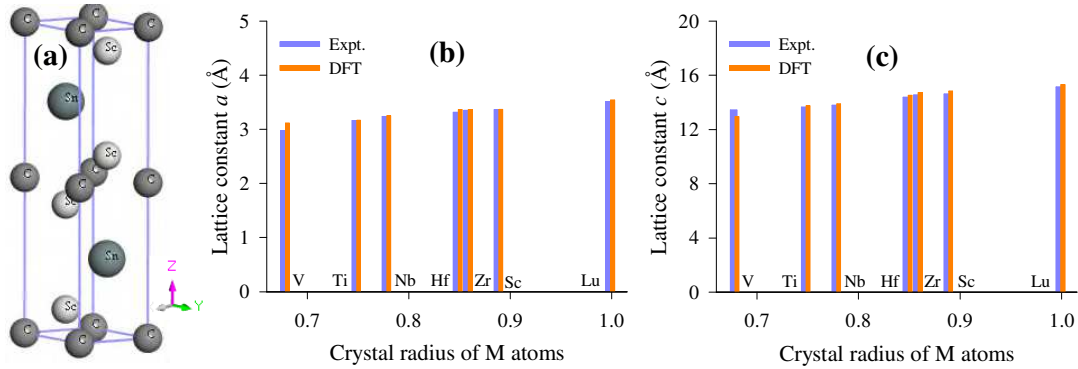


Figure 1. (a) Unit cell of Sc_2SnC ; (b) and (c) lattice constants as a function of crystal radius of M atoms.

Electronic properties:

Electronic band structure, electronic density of states (DOS), charge density map, Fermi surface, Mulliken population analysis are investigated to describe the electronic and bonding features of Sc_2SnC , a compound in M_2SnC MAX family.

Band structure and DOS: The electronic band structure of Sc_2SnC was calculated along the high symmetry directions in the first Brillouin zone and is shown in Figure 2a. It reveals the metallic characteristics of Sc_2SnC , which are similar to other MAX phases including M_2SnC as the valence band crosses the Fermi level E_F and overlaps with the conduction band. The Fermi level of Sc_2SnC intersects the crossing bands roughly along the middle and is located at about equal energies from both the pure valence and conduction bands. On the other hand, the Fermi level in V_2SnC and Ti_2SnC lies just below the valence band maximum nearby the Γ -point^{4,30}. The Γ -point, where most of the valence bands accumulate, shifts upwards for other M_2SnC MAX phases (see Fig. 6 in Ref. 4). The distance of this point from Fermi level increases following the order: $Ti_2SnC < V_2SnC < Nb_2SnC < Zr_2SnC < Hf_2SnC < Sc_2SnC < Lu_2SnC$. The band features of the Sc_2SnC are very similar to that of the Lu_2SnC compared to other M_2SnC phases⁴. A notable feature in the band structure is the considerably anisotropic nature with low energy dispersion along the c -axis. This is apparent from the reduced dispersion along the short H–K and M–L directions. The anisotropic nature of the band structure near and below the Fermi level indicates that the electrical conductivity is as anisotropic for the Sc_2SnC as for the other M_2SnC MAX phases.

To obtain more information on the chemical bonding in Sc_2SnC , the total and partial densities of states were calculated and are shown in Figure 2b. In this figure, the broken vertical green line refers to the Fermi level E_F , which is located to the left of a pseudogap in the total DOS. It is one of the indications of the structural stability of Sc_2SnC . The greater proximity of E_F to the pseudogap indicates greater structural stability of the compound. Comparing the position of E_F relative to the pseudogap for all existing M_2SnC MAX phases the structural stability should follow the order: Nb_2SnC

> Ti₂SnC > Lu₂SnC > Zr₂SnC > Hf₂SnC > Sc₂SnC > V₂SnC. The main contribution to the total DOS at E_F comes from the d orbital of Sc. The d-resonance at the surroundings of E_F and the finite value of the total DOS at E_F indicates the metallic character of Sc₂SnC and this is a common feature of MAX phases. The total DOS of Sc₂SnC at E_F is 3.10 states/eV-uc, which is about half of V₂SnC (6.12 states/eV-uc) and between the range (2.35 – 3.93 states/eV-uc) of other M₂SnC phases^{4,30}.

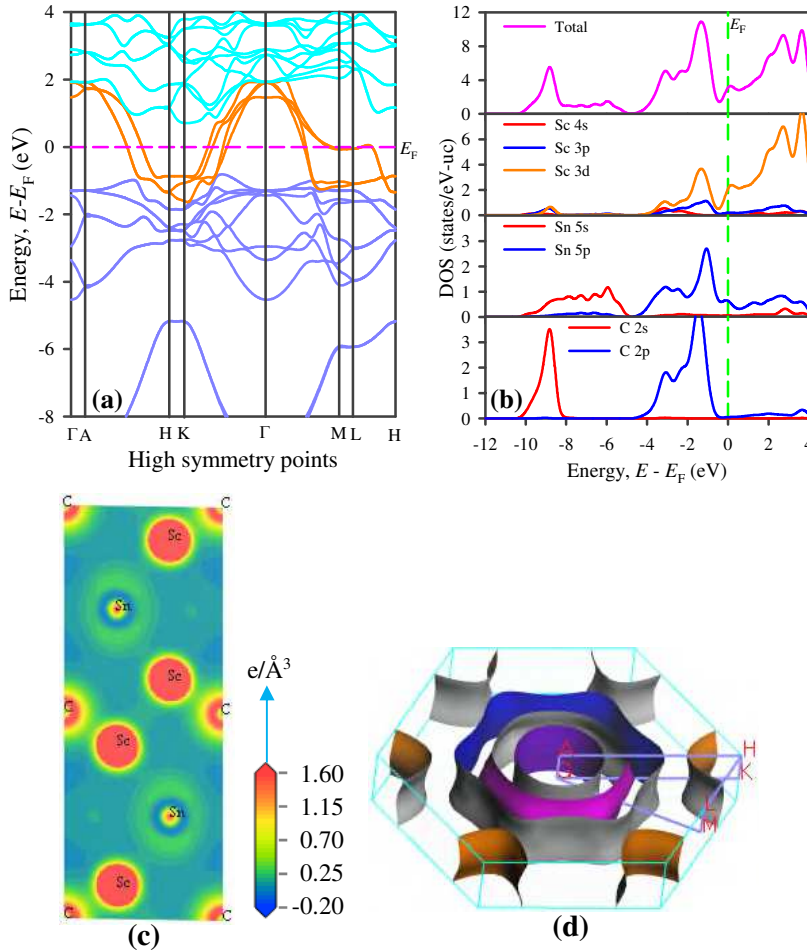


Figure 2. (a) Band structure, (b) Density of states, (c) Charge density map and (d) Fermi surface of Sc₂SnC.

The valence band of Sc₂SnC is divided into two main parts. The lower part is situated between –10.4 eV and –4.9 eV, which contains a distinct peak and a flat region. The peak originates as a result of hybridization between Sc 3d and C 2s orbitals, indicating covalent Sc–C bonding. The flat region arises due to the main contribution of Sn 5s electrons. The upper valence band consists of two distinct peaks. The highest peak close to E_F is also due to the hybridization of Sc 3d electrons with C 2p electrons. Hybridization between Sc 3p and Sn 5p near the E_F also contributes to the highest peak of the total DOS. This hybridization leads to the formation of the Sc–Sn covalent bond between Sc and Sn. This bond is not as strong as Sc–C because the corresponding peak is closer to the Fermi level. The lowest peak centered at –3.3 eV arises due to the interaction between Sc 3d and C 2p states. The bonding nature of Sc₂SnC is almost same of other M₂SnC MAX phases. Overall, the bonding character in Sc₂SnC is a combination of metallic, covalent, and, owing to the difference in electronegativity between the comprising elements, ionic like other MAX phase compounds.

Charge density: The contour map of the electron charge distribution among the comprising atoms in a compound is a way to understand the nature of atomic bonding in the material. The contour map for Sc₂SnC is given in Figure 2c. It can be observed that the charge distributions around the atoms have created an almost spherical electron cloud and its intensity determines the amount of charge accumulation. The amount of charge accumulated around the Sc atom is 0.53e, while the amount of charge accumulated around the M atom of other M₂SnC phases is between 0.28 – 0.45e^{4,30}. Clearly, the maximum charge accumulates around the Sc atom among all M-atoms in M₂SnC phases. The minimum charge is found to accumulate around Hf⁴. The electron cloud of Sc-charge overlaps with that of C-charge and slightly edges with that of Sn-charge, which indicates the stronger covalent Sc–C and weaker covalent Sc–Sn bonding, respectively. The spherical distribution of charge around the atoms is an indication of some ionic character in chemical bonds in Sc₂SnC. The contour map of electron charge distribution for Sc₂SnC is almost identical to those of other M₂SnC phases.

Fermi surface: The Fermi surface (FS) is a conceptual surface in reciprocal space that separates occupied electron states from unoccupied ones at zero temperature. The dynamical properties of an electron on the FS mostly depend on where it is located on the FS, and the shape of the FS with respect to the Brillouin zone can serve as a guide to the electrical properties of a metallic system. Currently, the presence of a FS is likely the utmost significant signature of the entity of Fermi liquid quasiparticles in a material. Indeed, the FS is related to a range of interesting physical phenomena. The FS of Sc₂SnC was calculated and is shown in Figure 2d. The FS consists of four Fermi sheets centered along the Γ –A direction. The three Fermi sheets close to the center of the Brillouin zone have cylindrical or prismatic-like hexagonal cross sections. These are 2D-like electron sheets. The remaining sheet consists of six separate parts parallel to the H-K directions. This sheet is hole-like and situated at the corners of the Brillouin zone around the H-K directions. In comparison to the FSs of M₂SnC family, the FS of Sc₂SnC is very similar to that of Lu₂SnC and simple enough compared to the FSs of other M₂SnC phases^{4,30}. The non-spherical shape of the Fermi sheets is an indication of the metallic conductivity of Sc₂SnC.

Mulliken population: Population analysis in CASTEP is carried out using a projection of the planewave (PW) states onto a linear combination of atomic orbitals (LCAO) localized basis using a method developed by Sanchez-Portal et al.³³. Population analysis of the resultant projected states is then accomplished using the Mulliken formalism³⁴. This analysis provides the Mulliken charge, bond population and bond length in a bulk material. Mulliken charge associated with a given atom, A, can be determined as:

$$Q(A) = \sum_k \omega_k \sum_{\mu}^{on A} \sum_v P_{\mu\nu}(k) S_{\mu\nu}(k) \quad (1)$$

where $P_{\mu\nu}(k)$ is the density matrix and $S_{\mu\nu}(k)$ is overlap matrix. The bond population between two atoms A and B can be calculated as:

$$P(AB) = \sum_k \omega_k \sum_{\mu}^{on A} \sum_v^{on B} 2P_{\mu\nu}(k) S_{\mu\nu}(k) \quad (2)$$

The Mulliken charge measures the effective valence from the absolute difference between the formal ionic charge and the Mulliken charge on the atomic species. Table S2 lists the effective valence, bond population, and bond length between different atoms in Sc₂SnC and existing M₂SnC MAX phases. The pure valence states for transition metals Sc, Ti, V, Zr, Nb, Lu, and Hf in M₂SnC MAX phases are 3d¹, 3d², 3d³, 4d², 4d⁴ 5s¹, 5d¹, 5d², respectively. It is observed that the effective valence largely depends on the d-orbital electrons of the transition metals. It increases when the transition metal moves from the left to the right in the periodic table. Its non-zero positive value is an indication of mixed covalent and ionic nature in chemical bonds. Its progression towards zero value indicates an increase in the level of ionicity. Its zero value implies an ideal ionic character in a

chemical bond. Its progression from zero with a positive value indicates an increase in covalency level of chemical bonds. Based on the effective valence the covalency of M_2SnC increase when M atoms move from the left to the right in the periodic table.

Bond population is another indication of bond covalency in a crystal as a high value of bond population in essence indicates a high degree of covalency in the chemical bond. The M–C bond in the MAX phases is mainly covalent bond. The bond population of M–C bond in each M_2SnC MAX phases is positive except in Lu_2SnC . The bond population of M–C bond in M_2SnC decreases when the M atom moves from the left to the right in the periodic table, indicating the decrease in covalency. Actually, effective valence and positive bond population combinedly control the covalency of crystalline solids. The bulk modulus is mostly controlled by the bond covalency. Between effective valence and positive bond population, which is most influential in bond covalency? This can be verified with the bulk modulus. It is observed from the Figure 4(a) in the next section that the bulk modulus changes according to the effective valence. Therefore, it can be concluded that the effective valence mainly controls the covalency level in a crystal. The bond length of covalent M–C bond decreases when the M atom moves from the left to the right in the periodic table. It is clear that the shorter the covalent bond length, the higher the bond covalency. A negative bond population indicates the antibonding state between two relevant atoms. Other bonds in M_2SnC MAX phases have negative bond population with the exception of the M-Sn bond in Sc_2SnC and the Sn–C bond in Lu_2SnC . Indeed, the Sn–C bond is the source of the covalency in Lu_2SnC .

Mechanical properties:

Single crystal elastic constants, bulk elastic moduli, elastic anisotropy, Vickers hardness are calculated to describe the mechanical behaviors of Sc_2SnC in comparison to existing M_2SnC phases.

Single crystal elastic constants: Elastic constants are the fundamental tools for accessing the mechanical behavior of crystalline solids. MAX phases have five independent elastic constants C_{ij} due to their hexagonal crystal symmetry. These are C_{11} , C_{33} , C_{44} , C_{12} and C_{13} . In addition they have one more dependent elastic constant C_{66} , which depends on C_{11} and C_{12} and $C_{66} = (C_{11} - C_{12})/2$. First of all, the elastic constants justify the mechanical stability of compounds obeying Born criteria. For hexagonal systems these criteria are as follows³⁵:

$$C_{11}, C_{33}, C_{44} > 0; C_{11} > |C_{12}| \text{ and } (C_{11} + C_{12})C_{33} > 2C_{13}C_{13} \quad (3)$$

The calculated elastic constants of Sc_2SnC are listed in Table S3 and shown in Fig. 3 along with CASTEP-derived elastic constants for existing M_2SnC phases for comparison. Sc_2SnC meets the above conditions by its elastic constants like its predecessors M_2SnC and ensures its own mechanical stability like its predecessors.

The elastic constants C_{11} and C_{33} represent the elasticity in length, whereas other constants such as C_{12} , C_{13} , and C_{44} are associated with elasticity in shape. Indeed, C_{11} and C_{33} represent the stiffness along the crystallographic a- and c-axis, respectively. The stiffness of Sc_2SnC is slightly larger along the a-axis than along the c-axis, which is also observed for Ti_2SnC , Nb_2SnC and Hf_2SnC . For the remaining M_2SnC phases, V_2SnC , Zr_2SnC , and Lu_2SnC , the stiffness along the c-axis is slightly larger than that in the a-axis. The difference between C_{11} and C_{33} quantifies the level of elastic anisotropy in crystals relating to the crystallographic axis. Accordingly, V_2SnC , Nb_2SnC , and Hf_2SnC are elastically more anisotropic than Sc_2SnC , Ti_2SnC , Zr_2SnC , and Lu_2SnC . The new phase Sc_2SnC ranks fourth in the view of both less and high anisotropy in the M_2SnC family of seven members.

Shear elastic constants C_{12} and C_{13} reciprocally lead to a functional stress component along the crystallographic a-axis with a uniaxial strain along the crystallographic b- and c-axis, respectively. This stress component takes the measurements of the shear deformation resistance of a compound along the crystallographic b- and c-axis, when stress is applied along the a-axis. The Nb_2SnC phase is most capable of resisting such deformation, whereas Lu_2SnC will easily deform under an equal stress along the a-axis. The new compound Sc_2SnC will be the second in rank in M_2SnC systems that will be

easily deformed if a rank of deformation resistance of M_2SnC system is made: $Nb_2SnC > V_2SnC > Hf_2SnC > Ti_2SnC > Zr_2SnC > Sc_2SnC > Lu_2SnC$.

Elastic constant C_{44} gives an indirect measure of the indentation hardness of a material. A low value of C_{44} indicates higher shearability and low hardness of a compound. High shearability and low hardness are related to better machinability of a compound. Due to low value of C_{44} , Lu_2SnC is the softest and most easily machinable among the seven M_2SnC MAX phases. The new material Sc_2SnC should be the second in rank in the M_2SnC systems that will be soft and easily machinable.

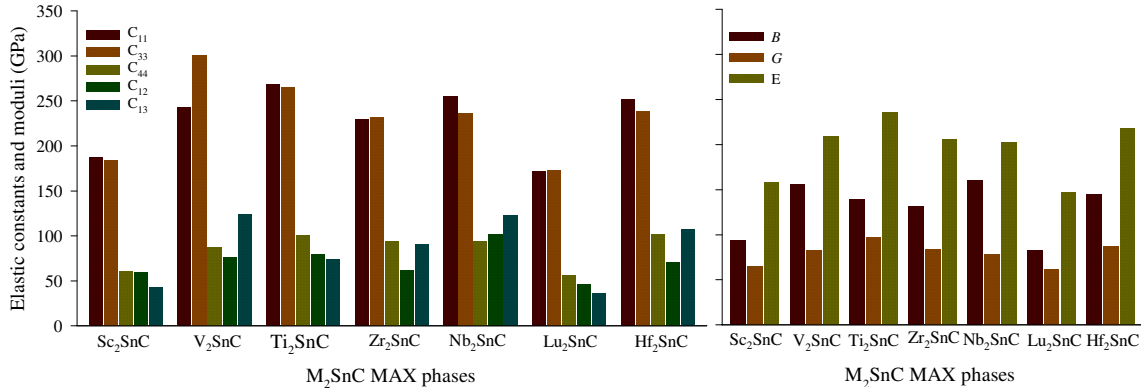


Figure 3. Elastic constants C_{ij} and moduli B , G , and E of Sc_2SnC and other MAX phases.

The symmetry condition $C_{66} = (C_{11} - C_{12})/2$ represents an important consequence in hexagonal crystals. C_{66} serves as the shear constant on the (100) plane in a [010] direction, while $(C_{11} - C_{12})/2$ stands for the shear constant on the (110) plane in a [110] direction. Therefore, the elastic shear constant is the same for all planes in the [001] zone, independent on the specific shear plane or shear direction, which known as transverse isotropy. This means that the elastic constants are invariant for arbitrary rotation around the z-axis: in the xy plane, the hexagonal crystals are elastically isotropic, which we will observe in a next section.

Bulk elastic moduli: Elastic moduli are the most important elastic parameters that assess the mechanical behavior of crystalline solids. Calculated elastic moduli are listed in Table S3 and shown in Figure 3. Bulk modulus B and shear modulus G can be derived from the elastic constants C_{ij} using Voight–Reuss–Hill approximations^{36–38}. A detailed discussion of these methods for hexagonal crystals is found in a recent study³⁹. The bulk modulus of a crystal depends microscopically on the nature of its bond such as length and type. It is also controlled by the total effective valence of the crystal (refer to Fig. 4a). Bulk modulus measures the resistance to uniform compression of a material and is highly linked to chemical composition and crystal structure. Among M_2SnC phases, the new phase Sc_2SnC possesses the second lowest value for B . The highest value is assigned to Nb_2SnC and the lowest value is associated with Lu_2SnC . Therefore, Sc_2SnC will be compressed easily compared to existing M_2SnC phases except Lu_2SnC . The shear modulus G is concerned with the deformation of a solid material when it experiences a force parallel to one of its surfaces while its opposite face experiences an opposing force such as friction. G maintains a good relationship with C_{44} . Here, it is reflected and Sc_2SnC secure the second rank in the scale of lowest value of G similar to C_{44} . Thus, Sc_2SnC should be easily machinable than other M_2SnC phases except Lu_2SnC .

B and G collectively prescribe an important parameter known as Pugh's ratio (defined as B/G) that evaluates a necessary mechanical behavior of crystalline solids⁴⁰. Generally, a material is either considered brittle or ductile. In some cases, some materials behave neutral. A neutral material has a Pugh's ratio of 1.75 while the brittle materials have a value less than 1.75 and ductile materials possess a value greater than 1.75. Accordingly, Sc_2SnC is a brittle material similar to Ti_2SnC , Zr_2SnC , Lu_2SnC and Hf_2SnC while V_2SnC and Nb_2SnC exhibit ductility (refer to Figure 4(b)).

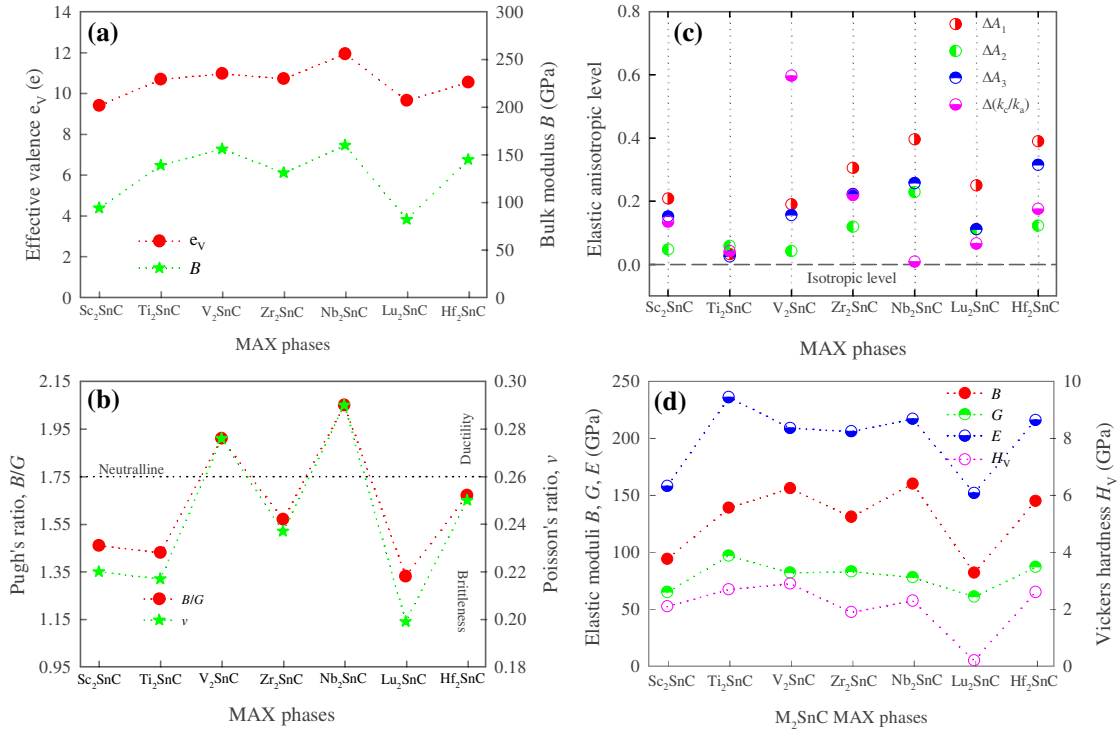


Figure 4. (a) Bulk modulus with effective valence; (b) Pugh's and Poisson's ratio; (c) elastic anisotropy level and (d) Vickers hardness with elastic moduli of M₂SnC.

Poisson's ratio ν is another important parameter and can be derived from B and G : $\nu = (3B - 2G)/(6B + 2G)$. Similar to Pugh's ratio, Poisson's ratio can serve as a predictor for distinguishing brittle and ductile materials from neutral ones. Poisson's ratio ν with a value of 0.26 identifies the neutral materials as well as with a lower value it finds out the brittle materials and with a higher value it seeks the ductile ones⁴¹. The Poisson's ratio has classified the M₂SnC MAX phases into brittle and ductile groups, just as the Pugh's ratio has classified them above. That is, the Sc₂SnC can be considered brittle. The Poisson's ratio can also identify the interatomic forces between atoms in a solid⁴². When the Poisson's ratio of a solid is between 0.25 – 0.50, the interatomic forces between the atoms of that solid will be the central forces. If the Poisson's ratio is outside of this range the interatomic forces will be the non-central forces. The Poisson's ratio of V₂SnC, Hf₂SnC and Nb₂SnC lies in this range and accordingly their interatomic forces are central forces. The interatomic forces in the new phase Sc₂SnC including remaining M₂SnC phases are non-central forces as their Poisson's ratios are outside this range. Moreover, the Poisson's ratio can predict the bonding nature in solids⁴³. A completely covalent crystal is characterized with a Poisson's ratio equal or less than 0.1. A perfectly metallic compound possesses a Poisson's ratio equal or greater than 0.33. The Poisson's ratio of Sc₂SnC including existing M₂SnC lies between 0.1 and 0.33, indicating that their chemical bonding is a combination of metallic and covalent natures.

Elastic moduli B and G also provide another essential property; the Young's modulus E through the equation, $E = 9BG/(3B + G)$. The Young's modulus of a material is a useful property for predicting the behaviour of the material when subjected to a tensile force. Stiffness of a material mostly depends on its Young's modulus. Higher Young's modulus is an indication of higher stiffness. In the family of M₂SnC MAX phases, Ti₂SnC is the stiffest material and Lu₂SnC is the softest one. The newly synthesized Sc₂SnC ranks second on the scale of softness: Lu₂SnC > Sc₂SnC > Nb₂SnC > Zr₂SnC > V₂SnC > Hf₂SnC > Ti₂SnC. Again, the larger the E value, the greater the exfoliation energy. Among the effectively etched MAX phases into 2D MXenes, V₂AlC has the largest exfoliation energy, whose E is reported to be 311 and 316 GPa^{44,45}. In view of that, the exfoliation energy of newly synthesized

Sc₂SnC and other M₂SnC phases have lower exfoliation energy than V₂AlC. Therefore, Sc₂SnC and other M₂SnC phases are more likely to be etched into 2D MXenes than V₂AlC. Further, the Young's modulus E has a good relation to the thermal shock resistance R : $R \propto 1/E^{46}$. The lower the Young's modulus, the better the thermal shock resistance. A material of higher thermal shock resistance (i.e., lower Young's modulus) has the potential to be used as a thermal barrier coating (TBC) material. The Young's modulus of newly synthesized Sc₂SnC and other M₂SnC MAX phases are lower than that of a potential TBC material TiO₂ whose Young modulus is 283 GPa⁴⁷. Therefore, Sc₂SnC and other existing M₂SnC phases have possibility to be TBC materials if they also have high thermal expansion coefficient and melting point, low thermal conductivity, and good oxidation resistance.

Elastic anisotropy: The study of elastic anisotropy is important in materials science as it influences a variety of physical processes including the development of plastic deformation in crystals, microscale cracking in ceramics, and plastic relaxation in thin-film metallics⁴⁸. For hexagonal crystals like MAX phases the shear anisotropy factors A_i ($i = 1, 2, 3$) are studied extensively^{21,22,25,31,49}. The equation that determines the shear anisotropy factor A_1 , for the {100} shear planes between the <011> and <010> directions, is $A_1 = (C_{11} + C_{12} + 2C_{33} - 4C_{12})/6C_{44}$; the equation of A_2 , for the {010} shear planes between <101> and <001> directions, is $A_2 = 2C_{44}/(C_{11} - C_{12})$; and the equation of A_3 , for the {001} shear planes between <110> and <010> directions, is $A_3 = (C_{11} + C_{12} + 2C_{33} - 4C_{13})/3(C_{11} - C_{12})$. Deviation of A_i from unity $\Delta A_i (= A_i \sim 1)$ quantifies the degree of the shear anisotropy of crystals. The calculated A_i is listed in Table S4 and the anisotropy level ΔA_i is shown in Figure 4c. Considering the average on the all planes, Ti₂SnC is elastically less anisotropic and Nb₂SnC is elastically highly anisotropic. Sc₂SnC ranks third in view of less anisotropy in the M₂SnC family: Nb₂SnC > Hf₂SnC > Zr₂SnC > Lu₂SnC > Sc₂SnC > V₂SnC > Ti₂SnC. Individually, in the {100} shear planes Nb₂SnC is highly anisotropic; in the {010} shear planes Nb₂SnC is again highly anisotropic and in the {001} shear planes Hf₂SnC is highly anisotropic.

The anisotropy level in the hexagonal crystals like MAX phases can also be quantified by another anisotropy factor named compressibility anisotropy factor and it is defined as $k_c/k_a = (C_{11} + C_{12} - 2C_{13})/(C_{33} - C_{13})$ ⁴¹. Here, k_a and k_c are the linear compressibility coefficients along the a - and c -axis, respectively. Deviation of k_c/k_a from the unity $\Delta(k_c/k_a) (= k_c/k_a \sim 1)$ quantifies the degree of the compressibility anisotropy of crystals. The calculated k_c/k_a is listed in Table S4 and $\Delta(k_c/k_a)$ is shown in Fig. 4c. The compressibility anisotropy level is highest in V₂SnC and lowest in Nb₂SnC. Sc₂SnC ranks in the middle in the M₂SnC family of seven members. If $k_c/k_a > 1$, the material is more compressible along the c -axis than along the a -axis. Therefore, Sc₂SnC, Ti₂SnC and Lu₂SnC are slightly more compressible along the c -axis than along the a -axis while V₂SnC, Zr₂SnC, Nb₂SnC and Hf₂SnC are compressed more easily along the a -axis than along the c -axis.

There are some anisotropy factors such as percentage anisotropy factors $A_{B\%}$ and $A_{G\%}$ based on the bulk and shear moduli within the Voigt and Reuss limits, which are applicable for all types of crystals. $A_{B\%}$ measures anisotropy in compression while $A_{G\%}$ measures anisotropy in shear. These two factors are defined as $A_{B\%} = [(B_V - B_R)/(B_V + B_R)] \times 100\%$ and $A_{G\%} = [(G_V - G_R)/(G_V + G_R)] \times 100\%$ ⁴³. The calculated values are listed in Table S4. Both these factors assign zero value for isotropic crystals and their positive values indicate the anisotropy level in crystals. $A_{B\%}$ is highest for V₂SnC and lowest for Ti₂SnC while $A_{G\%}$ is highest for Hf₂SnC and lowest for Ti₂SnC. Sc₂SnC ranks fourth on the $A_{B\%}$ scale and second on the $A_{G\%}$ scale in terms of minimum anisotropy. Universal anisotropy factor A^U is also applicable for all types of crystals. It is defined as $A^U = 5(G_V/G_R) + (B_V/B_R) - 6 \geq 0$ ³⁰. Its zero value corresponds to isotropic crystals and a positive value implies the anisotropy level in crystals. The calculated values are listed in Table S4. Hf₂SnC has the highest value of A^U and Ti₂SnC possesses the lowest value. Sc₂SnC has the second lowest value of A^U .

The 2D and 3D graphical representations of the directional elastic properties of materials are visualization of elastic anisotropy in crystals. ELATE is open-source software⁵⁰, which allows the direct visualization of anisotropy level in Young's modulus (E), linear compressibility (β), shear modulus (G) and Poisson's ratio (ν) on the 3D spherical plot, as well as 2D projections on the (xy), (xz) and (yz) planes. Uniform circular 2D and spherical 3D graphical representations are the indications of

isotropic nature of crystals. Above, it is predicted that the hexagonal crystals like MAX phases are elastically isotropic in the xy plane. It is evident that the 2D presentation of E , β , G and ν of Sc_2SnC in the xy plane in Fig. 5 are uniformly circular, indicating the isotropic nature of elastic properties of Sc_2SnC in xy plane. The 2D presentation of E , β , G and ν of Sc_2SnC in the xz and yz planes in Fig. 5 is indicating the elastic anisotropy of Sc_2SnC in those planes. The greater the deviation from the round shape, the higher the anisotropy level in the crystals in that plane.

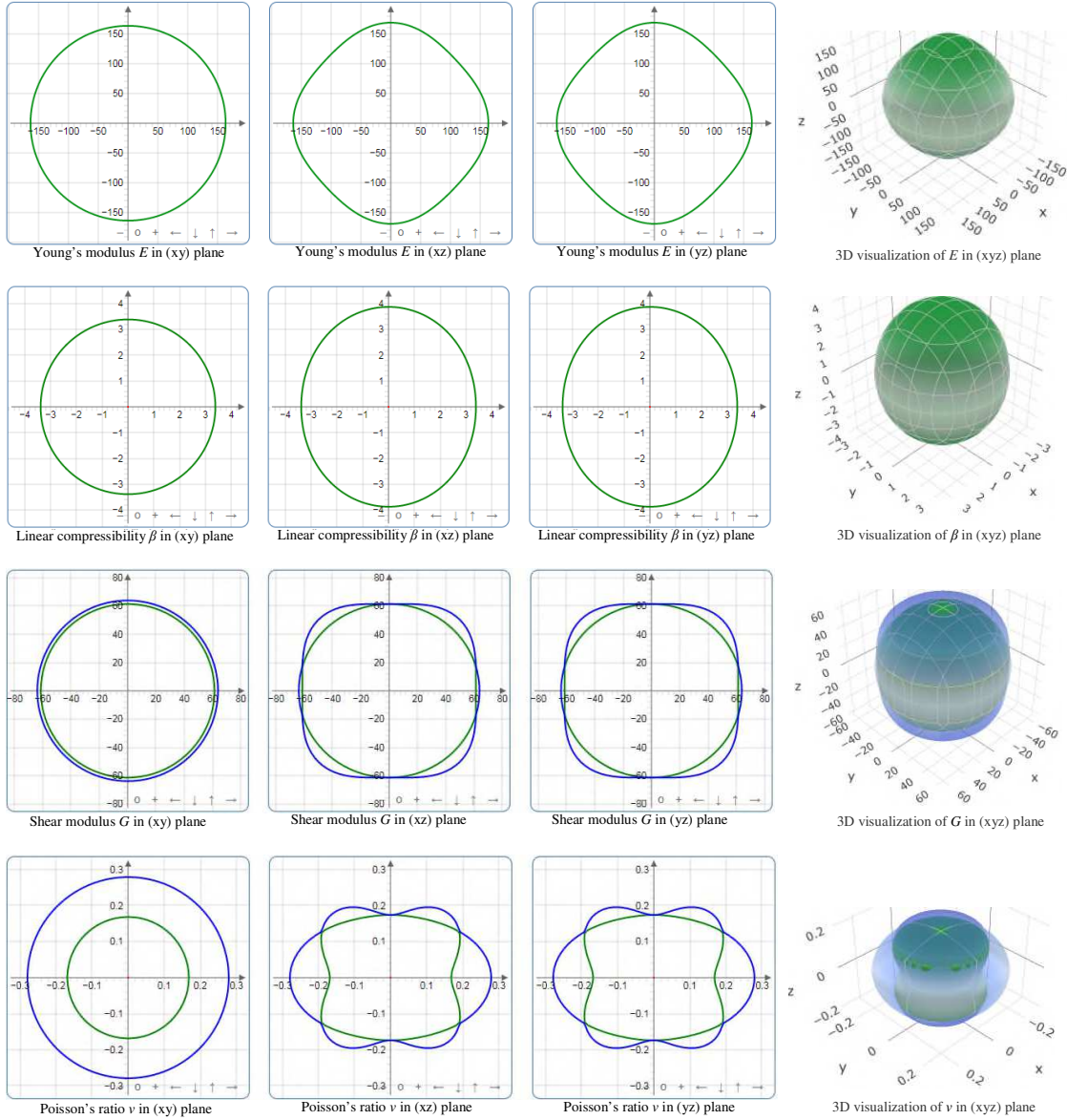


Figure 5. Directional dependence of Young's modulus (E), linear compressibility (β), shear modulus (G) and Poisson's ratio (ν) of Sc_2SnC .

In 2D and 3D presentations, ELATE uses maximum two colours for E and β and maximum three colours for G and ν . The E and β are functions of a single unit vector $\mathbf{a}(\vartheta, \phi)$ while G and ν depend on two orthogonal unit vectors $\mathbf{a}(\vartheta, \phi)$ and $\mathbf{b}(\vartheta, \phi, \chi)$ (\mathbf{a} in the direction of the stress applied while \mathbf{b} in the direction of measurement). The spherical coordinates ϑ , ϕ , and χ can be defined as $0 \leq \vartheta \leq \pi$, $0 \leq \phi \leq 2\pi$, and $0 \leq \chi \leq 2\pi$. Therefore, E , β , G and ν can be expressed as $E(\vartheta, \phi)$, $\beta(\vartheta, \phi)$, $G(\vartheta, \phi, \chi)$ and $\nu(\vartheta, \phi, \chi)$. $G(\vartheta, \phi, \chi)$ and $\nu(\vartheta, \phi, \chi)$ are represented in 3D space via plotting two surfaces f and g

each with the spherical (ϑ, ϕ) coordinates. The surfaces f and g represent the minimal and maximal values over all possible values of χ : $f(\vartheta, \phi) = \min_{\chi} X(\vartheta, \phi, \chi)$ and $g(\vartheta, \phi) = \max_{\chi} X(\vartheta, \phi, \chi)$, respectively. The surface g encloses the surface f . For this reason, g is plotted in translucent blue colour in Fig. 5. The surface f is represented with solid green color for positive values and translucent red color for negative values. The absence of red color implies that there are no negative values for E , β , G and ν of Sc_2SnC in any directions. The directional dependencies of E , β , G and ν on the xz and yz planes are almost identical for Sc_2SnC , similar to Nb_2SnC , Hf_2SnC and Zr_2SnC MAX phases³⁰. Ti_2SnC displays almost isotropic nature of E , β , G and ν in the xz and yz planes. The directional dependence of E , β , G , and ν in the Lu_2SnC differs from that of other M_2SnC phases. For Sc_2SnC , Ti_2SnC and Lu_2SnC , β has almost no directional dependence.

ELATE imparts a quantitative analysis reporting the minimum and maximum values of each modulus along with the directions along which these extrema occur. It also allows determining the directions of special interest for elastic properties, which are not required to be along the crystallographic axes of the material. Additionally, it reports a measurement of the anisotropy A_X of each elastic modulus X , which is defined below:

$$A_X = \begin{cases} X_{\max}/X_{\min} & \text{if } \text{sign}(X_{\max}) = \text{sign}(X_{\min}) \\ \infty & \text{otherwise} \end{cases} \quad (4)$$

The results are listed in Table 1. It is evident that Young's modulus exhibits maximum anisotropy for Nb_2SnC and minimum for Ti_2SnC and Sc_2SnC ranks second in view of minimum anisotropy. Anisotropy in linear compressibility is maximum for V_2SnC and minimum for Ti_2SnC ; Sc_2SnC ranks third in scale of minimum anisotropy. Anisotropy in shear modulus is highest for Hf_2SnC and lowest for Ti_2SnC ; Sc_2SnC ranks second in view of minimum anisotropy. Maximum anisotropy of Poisson's ratio is observed in Hf_2SnC and minimum in Ti_2SnC , whereas Sc_2SnC ranks third in view of minimum anisotropy. The lowest anisotropy is observed for Ti_2SnC in the M_2SnC family considering all indicators.

Table 1. Minimal and maximal values of each modulus and elastic anisotropy of Sc_2SnC and existing M_2SnC ^{30,31}.

Phases	Young's modulus (GPa)		Linear compressibility (TPa ⁻¹)		Shear modulus (GPa)		Poisson's ratio	
	E_{\min}	E_{\max}	β_{\min}	β_{\max}	G_{\min}	G_{\max}	ν_{\min}	ν_{\max}
Sc_2SnC	152.13	168.70	3.383	3.868	61.388	70.888	0.174	0.279
V_2SnC	188.79	223.85	1.096	2.711	71.355	86.673	0.129	0.388
Hf_2SnC	168.97	236.44	1.958	2.481	66.846	99.802	0.122	0.390
Lu_2SnC	143.59	167.39	3.831	3.959	56.841	70.092	0.166	0.264
Nb_2SnC	168.47	237.13	1.778	2.149	66.303	97.202	0.153	0.417
Ti_2SnC	233.72	239.43	2.415	2.451	95.408	100.210	0.194	0.225
Zr_2SnC	174.63	222.77	2.140	2.789	68.418	94.736	0.136	0.338
Elastic anisotropy A_X								
	A_E		A_β		A_G		A_ν	
Sc_2SnC	1.109		1.143		1.155		1.605	
V_2SnC	1.186		2.473		1.215		3.022	
Hf_2SnC	1.399		1.267		1.493		3.195	
Lu_2SnC	1.166		1.033		1.233		1.589	
Nb_2SnC	1.408		1.208		1.466		2.730	
Ti_2SnC	1.024		1.015		1.050		1.159	
Zr_2SnC	1.276		1.303		1.385		2.483	

Theoretical hardness: Hardness is the property of a material that facilitates it to resist plastic deformation, penetration, indentation and scratching. Therefore, hardness is important from an

engineering point of view because the resistance to wear by either abrasion or corrosion by steam, oil and water usually increases with hardness. Theoretical modeling for hardness calculation of partially metallic compounds like ternary MAX phases is difficult. Gou et al. developed a model⁵¹ based on Mulliken bond population³⁴ that is able to calculate the theoretical Vickers hardness of MAX phases. According to this model the bond hardness can be calculated as:

$$H_v^\mu = 740 (P^\mu - P^{\mu'}) (v_b^\mu)^{-5/3} \quad (5)$$

where P^μ denotes to the positive Mulliken bond overlap population of the μ -type bond, $P^{\mu'}$ represents the metallic population that is derived from the unit cell volume V and the number of free electrons in the cell, n_{free} with the formula, $P^{\mu'} = \frac{n_{free}}{V}$, here $n_{free} = \int_{E_P}^{E_F} N(E) dE$ and E_P and E_F define the energy at the pseudogap and at the Fermi level, respectively, and v_b^μ is the bond volume of a μ -type bond calculated using the equation $v_b^\mu = (d^\mu)^3 / \sum_\mu [(d^\mu)^3 N_b^\mu]$, here d^μ and N_b^μ are respectively the bond length and bond number of μ type bonds per unit volume.

When a compound has a positive bond population for multiple bonds, the following equation is used to calculate its Vickers hardness:

$$H_v = [\prod^\mu (H_v^\mu)^{n^\mu}]^{1/\sum n^\mu} \quad (6)$$

where n^μ represents the number of μ -type bonds. Table S5 lists the Vickers hardness of Sc_2SnC and other M_2SnC MAX phases. Sc_2SnC is harder than Lu_2SnC and Zr_2SnC and softer than Ti_2SnC , V_2SnC , Nb_2SnC and Hf_2SnC . We have found two sets of experimental Vickers hardness for Ti_2SnC , Zr_2SnC , Hf_2SnC , and Nb_2SnC ^{32,52}. Experimental values show deviations from one set to another except for Ti_2SnC . This can be due to sample purity and errors induced by the instruments. The experimental temperature may be another reason. Although the theoretical values deviate from the experimental values they remain within the typical values (2 – 8 GPa) for MAX phases. Lu_2SnC has a low value for H_v , which is very small compared to the lower limit (2 GPa) for the MAX phases. The reason may be the absence of covalent M–C bond in Lu_2SnC . Indeed, all M_2SnC phases have low hardness compared to most of the MAX phases. Consequently, M_2SnC phases are easily machinable compared to other MAX phases.

In general, the hardness of a compound has a better relationship with its shear and Young's modulus than bulk modulus³. We have plotted the Vickers hardness of M_2SnC MAX phases in Fig. 4d along with their elastic moduli. For the M_2SnC MAX phases, it is observed that the hardness follows the trend of bulk modulus instead of shear and Young's modulus. Further verification is needed to determine whether this trend continues for the carbide MAX phase with a specific A-group element.

Lattice dynamics:

The subject of lattice dynamics is the study of the vibrations of the atoms in a crystal. The vibrations of the atoms are related to many important physical properties such as lattice thermal conductivity, minimum thermal conductivity, Debye temperature, melting point, phonon dispersion, phonon DOS etc. These properties are investigated for newly synthesized Sc_2SnC to compare with existing M_2SnC phases

Debye temperature: Debye temperature is a characteristic temperature at which the highest-frequency mode (and hence every possible mode) is excited. It is related to many physical properties such as thermal expansion, thermal conductivity, specific heat and lattice enthalpy. Anderson method is simple and rigorous for calculating the Debye temperature of crystalline materials and uses the following equation⁵³:

$$\theta_D = \frac{h}{k_B} \left[\left(\frac{3n}{4\pi} \right) \frac{N_A \rho}{M} \right]^{1/3} v_m \quad (7)$$

All symbols bear the traditional meanings and v_m refers to the average sound velocity, which can be determined using the following equation:

$$v_m = \left[\frac{1}{3} \left(\frac{1}{v_l^3} + \frac{2}{v_t^3} \right) \right]^{-1/3} \quad (8)$$

Here, v_l and v_t are the longitudinal and transverse sound velocities, respectively. They can be calculated from the bulk and shear moduli B and G using the equations:

$$v_l = \left(\frac{3B + 4G}{3\rho} \right)^{1/2} \quad \text{and} \quad v_t = \left(\frac{G}{\rho} \right)^{1/2} \quad (9)$$

The calculated values of ϑ_b for $M_2\text{SnC}$ MAX phases are listed in Table S6 along with the relevant quantities. The Debye temperature of Sc_2SnC is the third highest in the $M_2\text{SnC}$ family. In this family, Ti_2SnC possesses the highest Debye temperature and Lu_2SnC has the lowest Debye temperature. The Debye temperature of $M_2\text{SnC}$ phases largely depends on the sound velocities and follows the trend of change of sound velocities with the transition metal M (refer to Fig. 6a).

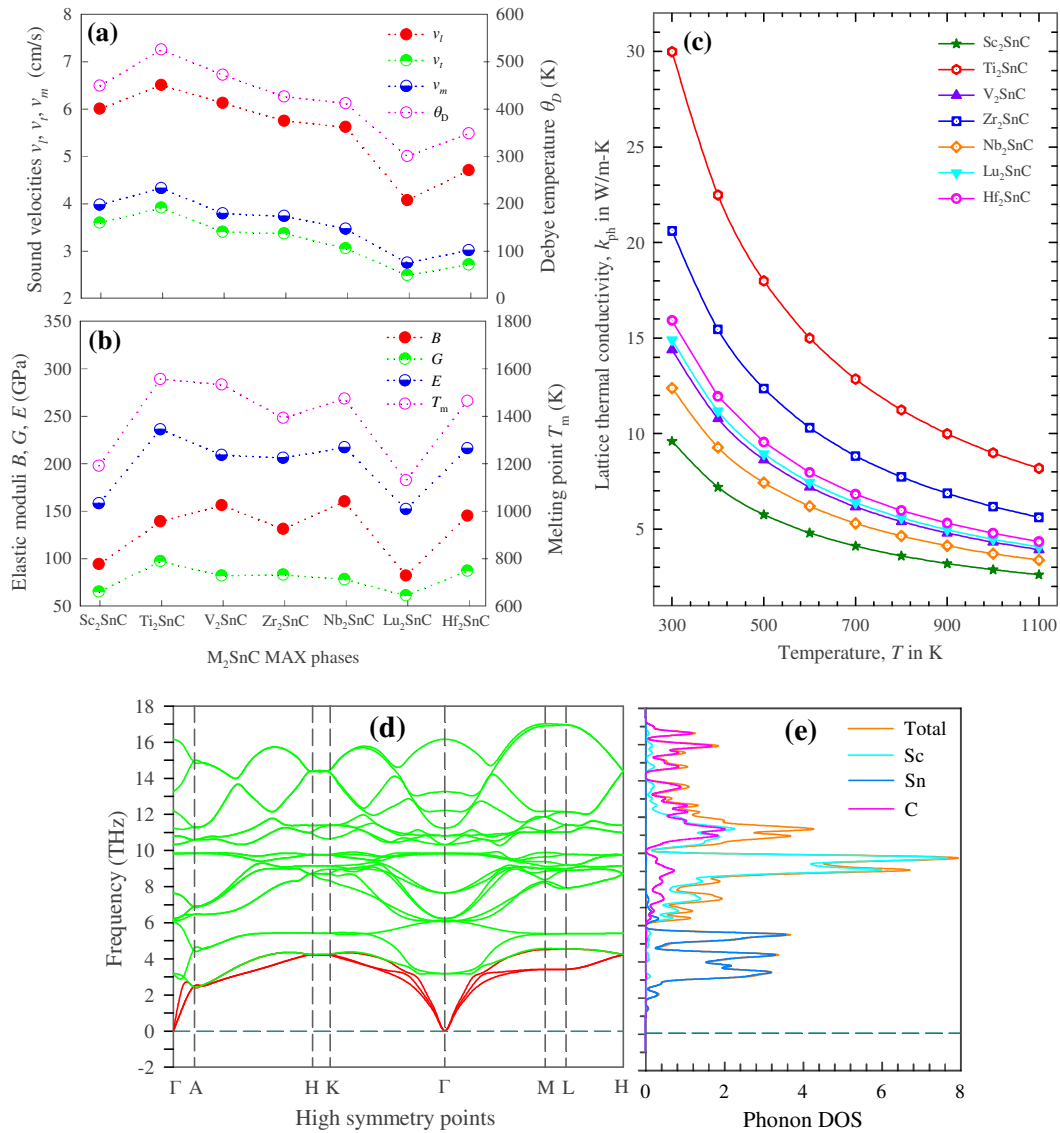


Figure 6. (a) Debye temperature with sound velocities; (b) melting temperature with elastic moduli; (c) lattice thermal conductivity as function of temperature; (d) phonon dispersion and (e) Phonon DOS.

Melting point: Melting point of hexagonal crystals like MAX phases can be calculated from elastic constants using: $T_m = 354 + 1.5(2C_{11} + C_{33})^{54}$. The calculated values are listed in Table S6. The new phase Sc_2SnC possesses the second lowest melting point. The highest melting point is obtained for Ti_2SnC and the lowest melting point is observed for Lu_2SnC . A higher melting point indicates greater interatomic forces in crystals. Interatomic forces mostly control the bulk elastic properties of crystalline solids. Thus, a relationship can exist between the elastic modulus and the melting temperature of the crystals. Considering this we plotted the elastic moduli and the melting point of M_2SnC MAX phases in Fig. 6(b). It is observed that the melting point has better correlation with bulk modulus B and Young's modulus E than shear modulus G .

Lattice thermal conductivity: The lattice thermal conductivity arises from contributions by phonons of all frequencies. The knowledge of lattice thermal conductivity is important to determine the applicability of a material for use in high temperature environments. Here, the Slack model is used to calculate the lattice thermal conductivity of Sc_2SnC as MAX phases have dual characteristics of metals and ceramics⁵⁵. The following equation is used in this model:

$$k_{ph} = A \frac{M_{av} \theta_D^3 \delta}{\gamma^2 n^{2/3} T} \quad (10)$$

The details of this model are found in a recent literature⁵⁶. The room temperature lattice thermal conductivity of Sc_2SnC and other M_2SnC phases are listed in Table S6 and their temperature dependency is shown in Fig. 6(c). It is observed that the new phase Sc_2SnC has the lowest lattice thermal conductivity in the entire temperature range and Ti_2SnC possesses the highest values for lattice thermal conductivity. The lattice thermal conductivity of M_2SnC MAX phases decrease gradually with the increase of temperature. The rate of decrease is slower for the Sc_2SnC phase and faster for the Ti_2SnC phase. Sc_2SnC should be most suitable candidate for thermal barrier coating (TBC) material due to its low lattice thermal conductivity.

Minimum thermal conductivity: Thermal conductivity decreases with increasing temperature. Thus, the minimum value of thermal conductivity is significant for the application of materials at high temperature conditions, for instance, materials selection and design for thermoelectric, thermal barrier coating and other thermal management applications. The concept of a minimum thermal conductivity, κ_{min} , carried by the atomic vibrations of any solid material leads to development of different models to determine it. Clarke model has become popular for determining the minimum thermal conductivity of solids via the equation⁵⁷:

$$\kappa_{min} = k_B v_m \left(\frac{n N_A \rho}{M} \right)^{2/3} \quad (11)$$

All symbols in equation (11) are consistent to the symbols used in equation (7). The calculated value of κ_{min} is listed in Table S6. The phase Sc_2SnC has the third highest value for κ_{min} . The highest value is found for V_2SnC and the lowest value is observed for Lu_2SnC . The ultralow minimum thermal conductivity of 1.25 W/m-K is used for screening the appropriate materials for TBC application⁵⁸. The values of κ_{min} for M_2SnC MAX phases are closer or lower than this optimum value. Therefore, all M_2SnC phases should be promising TBC materials with greater possibility for Lu_2SnC .

Phonon dispersion and Phonon DOS: It is important to study the phonon dispersion and phonon density of states (DOS) to verify the dynamical stability of the crystalline solids. The calculated phonon dispersion is shown in Figure 6(d). For a dynamically stable crystal, there are always three phonons with zero frequency at Γ -point, which corresponds to $k = 0$ in the reciprocal space. The phonon branches starting at $\omega(k) = 0$ are called acoustic phonon dispersion curves. In the case of Sc_2SnC (refer to Figure 6(d)) the acoustic branches start at $\omega(k) = 0$ and consequently indicates the dynamical stability of Sc_2SnC . Other phonons, whose frequencies are non-zero at the Γ point, are called optical phonons. In a number of high-symmetry crystals, and along the high-symmetry

directions, the atomic vibrations are either polarized along the propagation wave vector k , or perpendicular to k . Acoustic modes have one longitudinal acoustic (LA) mode, and two transverse acoustic (TA) modes. A crystal consisting of a unit cell of N -atoms has $3N - 3$ optical modes. 211 MAX phases have 21 optical modes. In the Fig. 6(d), the acoustic branches are shown with red and optical branches are identified with green.

The calculated phonon DOS of Sc_2SnC is shown in Figure 6(e), revealing that the acoustic and the lower optical modes arise due to the vibration of heavier Sn-atoms. The middle optical branches arise due to vibration of Sc-atoms. The higher optical branches mostly originate from the vibration of lighter C-atoms. Acoustic phonon is caused by the coherent vibrations of atoms in a lattice outside their equilibrium position. Conversely, the optical phonon is originated due to the out-of-phase oscillation of the atom in the lattice when an atom moves to the left and its neighbor to the right. Most of the optical properties of the crystals are controlled by the optical phonons.

Defect processes: The motivation to examine the point defect processes of materials stems from the fact that they can impact the macroscopic materials properties (i.e. radiation tolerance)^{59–61}. In that respect the investigation of point defects in MAX phases is very important as they can be in radiation environments given that they are considered for nuclear applications^{62–64}.

Table 2. The defect reaction energies as calculated for Sc_2SnC and existing M_2SnC ^{4,30} MAX phases.

	Reaction (\checkmark denotes vacancy)	Defect energy (eV)						
		Sc_2SnC	V_2SnC	Lu_2SnC	Ti_2SnC	Zr_2SnC	Hf_2SnC	Nb_2SnC
1.	$\text{M}_\text{M} \rightarrow \checkmark_\text{M} + \text{M}_\text{i}$	7.35	6.40	6.61	8.75	8.66	9.34	8.70
2.	$\text{Sn}_\text{Sn} \rightarrow \checkmark_\text{Sn} + \text{Sn}_\text{i}$	4.21	7.95	3.57	8.97	6.63	7.51	7.56
3.	$\text{C}_\text{C} \rightarrow \checkmark_\text{C} + \text{C}_\text{i}$	3.33	5.12	2.23	6.10	5.34	4.68	5.18
4.	$\text{M}_\text{M} + \text{Sn}_\text{Sn} \rightarrow \text{M}_\text{Sn} + \text{Sn}_\text{M}$	3.98	4.67	3.67	4.92	4.83	4.72	5.12
5.	$\text{M}_\text{M} + \text{C}_\text{C} \rightarrow \text{M}_\text{C} + \text{C}_\text{M}$	11.31	9.37	11.79	12.81	15.40	16.37	12.64
6.	$\text{Sn}_\text{Sn} + \text{C}_\text{C} \rightarrow \text{Sn}_\text{C} + \text{C}_\text{Sn}$	8.52	8.64	7.75	9.98	9.64	10.07	10.05
7.	$\text{Sn}_\text{i} + \checkmark_\text{M} \rightarrow \text{Sn}_\text{M}$	-4.57	-5.17	-3.61	-6.86	-4.71	-5.17	-4.34
8.	$\text{C}_\text{i} + \checkmark_\text{M} \rightarrow \text{C}_\text{M}$	-1.65	-0.80	-0.13	-1.07	0.12	1.47	-0.48
9.	$\text{M}_\text{i} + \checkmark_\text{Sn} \rightarrow \text{M}_\text{Sn}$	-3.01	-4.51	-2.90	-5.94	-5.75	-6.96	-6.79
10.	$\text{C}_\text{i} + \checkmark_\text{Sn} \rightarrow \text{C}_\text{Sn}$	1.26	0.03	1.56	-0.19	0.22	0.89	-0.10
11.	$\text{M}_\text{i} + \checkmark_\text{C} \rightarrow \text{M}_\text{C}$	2.27	-1.35	3.08	-0.97	1.28	0.88	-0.76
12.	$\text{Sn}_\text{i} + \checkmark_\text{C} \rightarrow \text{Sn}_\text{C}$	-0.29	-4.46	0.39	-4.91	-2.55	-3.01	-2.58
13.	$\text{M}_\text{i} + \text{Sn}_\text{Sn} \rightarrow \text{M}_\text{Sn} + \text{Sn}_\text{i}$	1.20	3.44	0.67	3.03	0.88	0.55	0.76
14.	$\text{M}_\text{i} + \text{C}_\text{C} \rightarrow \text{M}_\text{C} + \text{C}_\text{i}$	5.61	3.77	5.31	5.13	6.62	5.56	4.42
15.	$\text{Sn}_\text{i} + \text{M}_\text{M} \rightarrow \text{Sn}_\text{M} + \text{M}_\text{i}$	2.78	1.24	3.01	1.89	3.95	4.17	4.36
16.	$\text{Sn}_\text{i} + \text{C}_\text{C} \rightarrow \text{Sn}_\text{C} + \text{C}_\text{i}$	3.04	0.66	2.62	1.19	2.79	1.67	2.60
17.	$\text{C}_\text{i} + \text{M}_\text{M} \rightarrow \text{C}_\text{M} + \text{M}_\text{i}$	5.70	5.60	6.49	7.69	8.78	10.81	8.22
18.	$\text{C}_\text{i} + \text{Sn}_\text{Sn} \rightarrow \text{C}_\text{Sn} + \text{Sn}_\text{i}$	5.47	7.98	5.13	8.79	6.85	8.40	7.46
	Schottky reaction	9.78	5.83	9.99	7.97	9.69	8.57	6.70

Table 2 lists the defect reactions and the corresponding defect energies for Sc_2SnC and the existing M_2SnC MAX phases. In these calculations we have considered all the possible point defects including all the interstitial sites existing in the 211 M_2SnC MAX phases. For the defect reactions we employed the Kröger-Vink notation⁶⁵. In this notation M_i stands for an M interstitial defect, \checkmark_Sn for a Sn vacant site and M_Sn an M atom residing in a Sn site (known as antisite defect). Typically, the energies of the Schottky reaction in this system are high (Table 2) and therefore the Frenkel

reactions (Table 2, relations 1–3) or the antisite reactions (Table 2, relations 4–6) are more relevant when considering the radiation tolerance of the material. For Sc_2SnC the C-Frenkel energy is only 3.33 eV inferring that this is not a particularly radiation tolerant MAX phase as compared to most of the other MAX phases considered here (Table 2). Commonly, with the other MAX phases in Table 2 there is the possibility to form antisite vacancies via the recombination of self-interstitials and vacancies. For Sc_2SnC this is inferred by the negative energies in reactions 7–9 and 12.

Conclusions

In summary, we have employed DFT calculations to investigate the structural, electronic, mechanical and lattice dynamical properties of Sc_2SnC including defect processes to compare with those of existing M_2SnC MAX phases. The calculated structural properties show fair agreement with the experimental values. The structural, mechanical and dynamical stability of Sc_2SnC is verified. The chemical bonding of Sc_2SnC is a combination of metallic, covalent and ionic. The softness, machinability, elastic anisotropy level and deformability of Sc_2SnC are moderate compared to the other M_2SnC phases. Sc_2SnC has the potential to be etched into 2D MXenes and be a promising TBC material, similar to the other M_2SnC phases. The hardness of M_2SnC , including Sc_2SnC , follows the trend of bulk modulus rather than shear and Young's modulus while the melting point has a better relationship with the bulk and Young's modulus than with the shear modulus. The rate of declination of lattice thermal conductivity with temperature is slower for the Sc_2SnC phase and faster for the Ti_2SnC phase. Examining the defect processes of the existing M_2SnC phases it is revealed that Sc_2SnC is less radiation tolerant than numerous 211 MAX phases.

References

1. Nowotny, V. H. Strukturchemie einiger Verbindungen der Übergangsmetalle mit den elementen C, Si, Ge, Sn. *Progress in Solid State Chemistry* **5**, 27–70 (1971).
2. Barsoum, M. W. MAX Phases. (2013)
3. Hadi, M. A. Superconducting phases in a remarkable class of metallic ceramics. *Journal of Physics and Chemistry of Solids* **138**, 109275 (2020).
4. Hadi, M. A., Kelaidis, N., Naqib, S. H., Chroneos, A. & Islam, A. K. M. A. Electronic structures, bonding natures and defect processes in Sn-based 211 MAX phases. *Computational Materials Science* **168**, 203–212 (2019).
5. Zapata-Solvas, E. *et al.* Synthesis and physical properties of $(\text{Zr}_{1-x}\text{Ti}_x)_3\text{AlC}_2$ MAX phases. *Journal of the American Ceramic Society* **100**, 3393–3401 (2017).
6. Shuck, C. E. & Gogotsi, Y. MXenes: A Tunable Family of 2D Carbides and Nitrides with Diverse Applications. *Material Matters* **15**, 3–10 (2020).
7. Zhao, S. *et al.* Electrochemical Interaction of Sn-Containing MAX Phase (Nb_2SnC) with Li-Ions. *ACS Energy Lett.* **4**, 2452–2457 (2019).
8. Xu, Q. *et al.* Theoretical prediction, synthesis, and crystal structure determination of new MAX phase compound V_2SnC . *Journal of Advanced Ceramics* **9**, 481–492 (2020).
9. Chen, K. *et al.* MAX phase Zr_2SeC and its thermal conduction behavior. *Journal of the European Ceramic Society* **41**, 4447–4451 (2021).
10. Li Youbing, Q. Y., Chen Ke, Chen Lu, Zhang Xiao, Ding Haoming, Li Mian, Zhang Yiming, Du Shiyu, Chai Zhifang, Huang Qing. Molten Salt Synthesis of Nanolaminated Sc_2SnC MAX Phase. *Journal of Inorganic Materials* **36**, 773–778 (2021).
11. Toth, L. E., Jeitschko, W. & Yen, C. M. The superconducting behavior of several complex carbides and nitrides. *Journal of the Less Common Metals* **10**, 29–32 (1966).
12. Clark, S. J. *et al.* First principles methods using CASTEP: *Zeitschrift für Kristallographie - Crystalline Materials* **220**, 567–570 (2005).
13. Perdew, J. P., Burke, K. & Ernzerhof, M. Generalized Gradient Approximation Made Simple. *Phys. Rev. Lett.* **77**, 3865–3868 (1996).

14. Vanderbilt, D. Soft self-consistent pseudopotentials in a generalized eigenvalue formalism. *Phys. Rev. B* **41**, 7892–7895 (1990).
15. Monkhorst, H. J. & Pack, J. D. Special points for Brillouin-zone integrations. *Phys. Rev. B* **13**, 5188–5192 (1976).
16. Fischer, T. H. & Almlof, J. General methods for geometry and wave function optimization. *J. Phys. Chem.* **96**, 9768–9774 (1992).
17. Murnaghan, F. D. *Finite Deformation of an Elastic Solid*. (Wiley, New York, 1951).
18. Hadi, M. A. *et al.* First-principles prediction of mechanical and bonding characteristics of new T2 superconductor Ta₅GeB₂. *physica status solidi (b)* **253**, 2020–2026 (2016).
19. Hadi, M. A. *et al.* Elastic and thermodynamic properties of new (Zr_{3-x}Ti_x)AlC₂ MAX-phase solid solutions. *Computational Materials Science* **137**, 318–326 (2017).
20. Rubel, M. H. K. *et al.* Density functional theory study of a new Bi-based (K_{1.00})(Ba_{1.00})₃(Bi_{0.89}Na_{0.11})₄O₁₂ double perovskite superconductor. *Computational Materials Science* **138**, 160–165 (2017).
21. Roknuzzaman, M. *et al.* First hafnium-based MAX phase in the 312 family, Hf₃AlC₂: A first-principles study. *Journal of Alloys and Compounds* **727**, 616–626 (2017).
22. Nasir, M. T. *et al.* First-Principles Study of Superconducting ScRhP and ScIrP pnictides. *physica status solidi (b)* **254**, 1700336 (2017).
23. Christopoulos, S.-R. G. *et al.* Intrinsic defect processes and elastic properties of Ti₃AC₂ (A = Al, Si, Ga, Ge, In, Sn) MAX phases. *Journal of Applied Physics* **123**, 025103 (2018).
24. Tanveer Karim, A. M. M. *et al.* Newly synthesized MgAl₂Ge₂: A first-principles comparison with its silicide and carbide counterparts. *Journal of Physics and Chemistry of Solids* **117**, 139–147 (2018).
25. Hadi, M. A. *et al.* Physical properties and defect processes of M₃SnC₂ (M = Ti, Zr, Hf) MAX phases: Effect of M-elements. *Journal of Alloys and Compounds* **748**, 804–813 (2018).
26. Hadi, M. A., Islam, M. N. & Babu, M. H. Cubic Perovskite Pb(Mg_{1/3}Nb_{2/3})O₃: A Damage Tolerant, Machinable, and Thermal barrier coating material: *Zeitschrift für Naturforschung A* **74**, 71–81 (2019).
27. Filippatos, P. P. *et al.* 312 MAX Phases: Elastic Properties and Lithiation. *Materials* **12**, (2019).
28. Islam, M. N., Hadi, M. A. & Podder, J. Influence of Ni doping in a lead-halide and a lead-free halide perovskites for optoelectronic applications. *AIP Advances* **9**, 125321 (2019).
29. Ali, M. M. *et al.* DFT investigations into the physical properties of a MAB phase Cr₄AlB₄. *Journal of Alloys and Compounds* **821**, 153547 (2020).
30. Hadi, M. A. *et al.* Chemically stable new MAX phase V₂SnC: a damage and radiation tolerant TBC material. *RSC Adv.* **10**, 43783–43798 (2020).
31. Hadi, M. A., Kelaidis, N., Naqib, S. H., Chroneos, A. & Islam, A. K. M. A. Mechanical behaviors, lattice thermal conductivity and vibrational properties of a new MAX phase Lu₂SnC. *Journal of Physics and Chemistry of Solids* **129**, 162–171 (2019).
32. Barsoum, M. W., Yaroshuk, G. & Tyagi, S. Fabrication and characterization of M₂SnC (M = Ti, Zr, Hf and Nb). *Scripta Materialia* **37**, 1583–1591 (1997).
33. Sanchez-Portal, D., Artacho, E. & Soler, J. M. Projection of plane-wave calculations into atomic orbitals. *Solid State Communications* **95**, 685–690 (1995).
34. Mulliken, R. S. Electronic Population Analysis on LCAO–MO Molecular Wave Functions. I. *J. Chem. Phys.* **23**, 1833–1840 (1955).
35. Born, M. On the stability of crystal lattices. I. *Mathematical Proceedings of the Cambridge Philosophical Society* **36**, 160–172 (1940).
36. Voigt, W. *Lehrbuch der Kristallphysik*. (Taubner, Leipzig, 1928).
37. Reuss, A. Berechnung der Fließgrenze von Mischkristallen auf Grund der Plastizitätsbedingung für Einkristalle. *ZAMM - Journal of Applied Mathematics and Mechanics / Zeitschrift für Angewandte Mathematik und Mechanik* **9**, 49–58 (1929).

38. Hill, R. The Elastic Behaviour of a Crystalline Aggregate. *Proceedings of the Physical Society. Section A* **65**, 349–354 (1952).
39. Azzouz-Rached, A. *et al.* Pressure effects on the structural, elastic, magnetic and thermodynamic properties of Mn₂AlC and Mn₂SiC MAX phases. *Journal of Alloys and Compounds* **885**, 160998 (2021).
40. Pugh, S. F. XCII. Relations between the elastic moduli and the plastic properties of polycrystalline pure metals. *null* **45**, 823–843 (1954).
41. Hadi, M. A. New ternary nanolaminated carbide Mo₂Ga₂C: A first-principles comparison with the MAX phase counterpart Mo₂GaC. *Computational Materials Science* **117**, 422–427 (2016).
42. Hadi, M. A. *et al.* Effects of Al substitution by Si in Ti₃AlC₂ nanolaminate. *Scientific Reports* **11**, 3410 (2021).
43. Ali, M. A., Hadi, M. A., Hossain, M. M., Naqib, S. H. & Islam, A. K. M. A. Theoretical investigation of structural, elastic, and electronic properties of ternary boride MoAlB. *physica status solidi (b)* **254**, 1700010 (2017).
44. Aryal, S., Sakidja, R., Barsoum, M. W. & Ching, W.-Y. A genomic approach to the stability, elastic, and electronic properties of the MAX phases. *physica status solidi (b)* **251**, 1480–1497 (2014).
45. Cover, M. F., Warschkow, O., Bilek, M. M. M. & McKenzie, D. R. A comprehensive survey of M₂AX phase elastic properties. *Journal of Physics: Condensed Matter* **21**, 305403 (2009).
46. Wang, X. *et al.* Mechanical Properties and Damage Tolerance of Bulk Yb₃Al₅O₁₂ Ceramic. *Journal of Materials Science & Technology* **31**, 369–374 (2015).
47. Cao, X. Q., Vassen, R. & Stoeber, D. Ceramic materials for thermal barrier coatings. *Journal of the European Ceramic Society* **24**, 1–10 (2004).
48. Kube, C. M. Elastic anisotropy of crystals. *AIP Advances* **6**, 095209 (2016).
49. Hadi, M. A., Rayhan, M. A., Naqib, S. H., Chroneos, A. & Islam, A. K. M. A. Structural, elastic, thermal and lattice dynamic properties of new 321 MAX phases. *Computational Materials Science* **170**, 109144 (2019).
50. Gaillac, R., Pullumbi, P. & Coudert, F.-X. ELATE: an open-source online application for analysis and visualization of elastic tensors. *Journal of Physics: Condensed Matter* **28**, 275201 (2016).
51. Gou, H., Hou, L., Zhang, J. & Gao, F. Pressure-induced incompressibility of ReC and effect of metallic bonding on its hardness. *Appl. Phys. Lett.* **92**, 241901 (2008).
52. El-Raghy, T., Chakraborty, S. & Barsoum, M. W. Synthesis and characterization of Hf₂PbC, Zr₂PbC and M₂SnC (M=Ti, Hf, Nb or Zr). *Journal of the European Ceramic Society* **20**, 2619–2625 (2000).
53. Anderson, O. L. A simplified method for calculating the debye temperature from elastic constants. *Journal of Physics and Chemistry of Solids* **24**, 909–917 (1963).
54. Fine, M. E., Brown, L. D. & Marcus, H. L. Elastic constants versus melting temperature in metals. *Scripta Metallurgica* **18**, 951–956 (1984).
55. Morelli, D. T. & Slack, G. A. High Lattice Thermal Conductivity Solids. in *High Thermal Conductivity Materials* (eds. Shindé, S. L. & Goela, J. S.) 37–68 (Springer New York, 2006). doi:10.1007/0-387-25100-6_2.
56. Ali, M. M., Hadi, M. A., Ahmed, I., Haider, A. F. M. Y. & Islam, A. K. M. A. Physical properties of a novel boron-based ternary compound Ti₂InB₂. *Materials Today Communications* **25**, 101600 (2020).
57. Clarke, D. R. Materials selection guidelines for low thermal conductivity thermal barrier coatings. *Surface and Coatings Technology* **163–164**, 67–74 (2003).
58. Liu, Y. *et al.* Discovery of ABO₃ perovskites as thermal barrier coatings through high-throughput first principles calculations. *null* **7**, 145–151 (2019).
59. Grimes, R. W. *et al.* The Effect of Ion Size on Solution Mechanism and Defect Cluster Geometry. *Berichte der Bunsengesellschaft für physikalische Chemie* **101**, 1204–1210 (1997).
60. Sickafus, K. E. *et al.* Radiation Tolerance of Complex Oxides. *Science* **289**, 748 (2000).

61. Chroneos, A., Rushton, M. J. D., Jiang, C. & Tsoukalas, L. H. Nuclear wastefrom materials: Atomistic simulation case studies. *Journal of Nuclear Materials* **441**, 29–39 (2013).
62. Horlait, D., Grasso, S., Chroneos, A. & Lee, W. E. Attempts to synthesise quaternary MAX phases $(Zr,M)_2AlC$ and $Zr_2(Al,A)C$ as a way to approach Zr_2AlC . *null* **4**, 137–144 (2016).
63. Zapata-Solvas, E. *et al.* Experimental synthesis and density functional theory investigation of radiation tolerance of $Zr_3(Al_{1-x}Si_x)C_2$ MAX phases. *J Am Ceram Soc* **100**, 1377–1387 (2017).
64. Hanson, W. A., Patel, M. K., Crespillo, M. L., Zhang, Y. & Weber, W. J. Influence of electronic vs nuclear energy loss in radiation damage of Ti_3SiC_2 . *Acta Materialia* **161**, 302–310 (2018).
65. Kröger, F. A. & Vink, H. J. Relations between the Concentrations of Imperfections in Crystalline Solids. in *Solid State Physics* (eds. Seitz, F. & Turnbull, D.) vol. 3, 307–435 (Academic Press, 1956).

Acknowledgements

The authors wish to acknowledge the High-Performance Computing (HPC) facility at Coventry University, Priory Street, Coventry CV1 5FB, UK for providing the computational facility to calculate the defect processes in newly synthesized Sc_2SnC MAX phase.

Author contribution

M.A.H. conceived the study and prepared all figures. M.A.H. and S.-R.G.C. carried out the calculations. M.A.H. and A.C. wrote the main manuscript text. All authors reviewed the manuscript.

Competing interests

The authors declare no competing interests.

Data Availability

Data will be provided on reasonable request.

Additional information

Supplementary Information The online version contains supplementary material available at <https://>

Correspondence and requests for materials should be addressed to M.A.H.

Supplementary Files

This is a list of supplementary files associated with this preprint. Click to download.

- [SupplementaryInformationSc2SnC.docx](#)